



Enhancement and directional control of light output of scintillators by using microlens arrays: A numerical simulation study

Yaozhen Guo, Di Yuan, Zhongrui Li, Chenyu Zhu, Zixuan Dai, Bo Liu *

Shanghai Key Laboratory of Special Artificial Microstructure Materials and Technology, School of Physics Science and Engineering, Tongji University, Shanghai 200092, PR China

ARTICLE INFO

Keywords:

Microlens array
Scintillator
Enhancement of light output
Control of directional emission

ABSTRACT

In this investigation, we have carried out the simulations of light output and the directionality of emission from scintillators coated with microlens arrays by using the ray-optics method. We systematically analyze the impact of an individual microlens at different positions on the light output intensity and the directional control, followed by an entire understanding of microlens arrays. It is found that microlens arrays can be used to increase the extraction efficiency and control the directionality of emission of scintillation light. The multiple reflections by the lateral and bottom surfaces play an important role. A comprehensive understanding of the impact of the ratio of width and thickness of a scintillator and the refractive index of microlens is presented and discussed in details. The maximum angle-integrated intensity could be obtained when the refractive index of microlens is slightly larger than that of scintillator. Simulations based on genetic algorithms can be used to efficiently design the parameters of microlens arrays with a specific target of a combination of emission angle and total emission intensity.

1. Introduction

Scintillators which can convert the energy of ionizing radiation into a number of photons in visible or near-visible range play an important role in the field of nuclear radiation detection, such as nuclear physics experiments, national security, nuclear medical imaging and dark matter detection [1–6].

In the practical applications, the light extraction efficiency of scintillators is limited by total internal reflection due to their high refractive indices, thus reducing the performance of detectors. In recent years, some schemes based on the microstructures such as photonic crystals [7–12], plasmonic lattices [13,14] have been proposed, which exhibit obvious benefits to the light extraction and directional emission control. However, the microstructures with sub-wavelength and wavelength scales usually exhibit significant wavelength-dependence due to the diffractive nature.

Microlens arrays (MLAs) with the individual microlens size of 10 to 100 μm could be used to control the light propagation based on geometrical optics, obtaining extensive applications in light emitting diodes, illumination, and collimating or focusing in imaging systems [15–18].

MLAs coated on the surface of scintillators can control the scintillation light output and control the directional emission. Such control process could be complicated since the propagation of light could be affected by the size and the interface of scintillators. In this paper, we have carried out the simulations based on the ray-optics method,

providing a comprehensive understanding of the critical factors of individual microlenses and their arrays affecting on the light output of scintillators.

2. Methods of structure design and numerical simulations

Fig. 1(a) is the schematic illustration of a scintillator (refractive index of n_1) coated with a square-packed MLA (refractive index of n_2) on its surface. The individual microlenses are hemispheres with a diameter of D . As shown in Fig. 1(b), a far-field receiver in the simulations is used to collect the data of light intensity of each point P which can be defined by a zenith angle (φ_z), an azimuth angle (θ_A) and a distance between the center of the scintillator and the receiver (r).

The numerical simulations based on the ray-optics method traverse all the ray vectors and use vectors to trace light rays. This method has a higher precision but is more computational load compared with the traditional Monte Carlo method [19]. An isotropic scintillation light source is set at the center of the scintillator. The light rays from the source have their optical paths defined by three-dimensional vectors. At boundaries or interfaces, the direction and intensity of the transmitted and the reflected light rays are calculated by a transformational matrix. The intensity of each light ray emitted per unit time is defined as I_0 . When its intensity becomes to be less than I_T which is set to be 3%

* Corresponding author.

E-mail address: lbo@tongji.edu.cn (B. Liu).

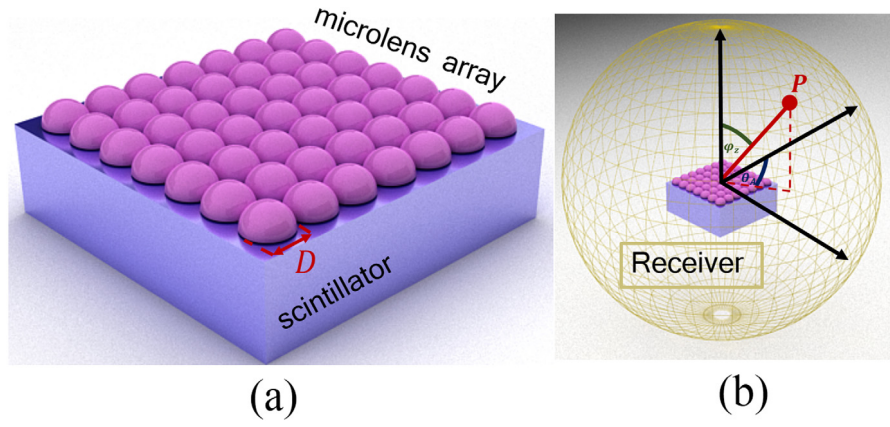


Fig. 1. (a) Schematic illustration of a scintillator coated with a microlens array on its surface. (b) Diagram of far-field detection.

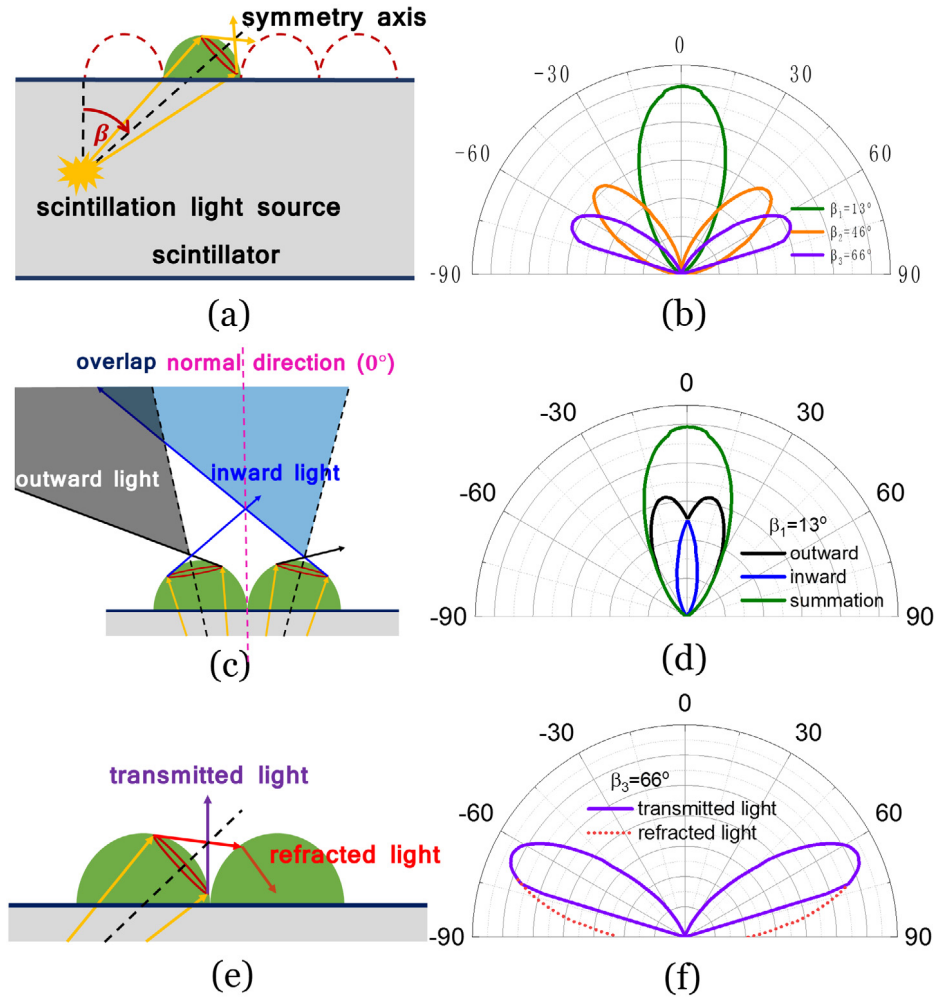


Fig. 2. (a) Definition of an individual microlens with its light ray paths. (b) Spatial distribution of light intensity for an individual microlens with representative angles of $\beta_1 = 13^\circ$, $\beta_2 = 46^\circ$ and $\beta_3 = 66^\circ$. (c) Schematic illustration of light ray paths for the inward light and the outward light for the range of β_1 . (d) Spatial distribution of light intensity of an individual microlens for $\beta_1 = 13^\circ$, including the inward light, the outward light and their summation. (e) Schematic illustration of light ray paths for the transmitted light and the refracted light for the range of β_3 . (f) Spatial distribution of light intensity of an individual microlens for $\beta_3 = 66^\circ$, including the transmitted light and the refracted light.

of I_0 , the calculation would be terminated. Finally, the data at each point P containing the information of the direction and intensity are recorded.

Genetic algorithms are used to obtain the optimal parameters [20]. A target parameter V is defined by the formula (1)

$$V = I_T(e^{\frac{I_{\theta_A}}{I_T}} - 1) \quad (1)$$

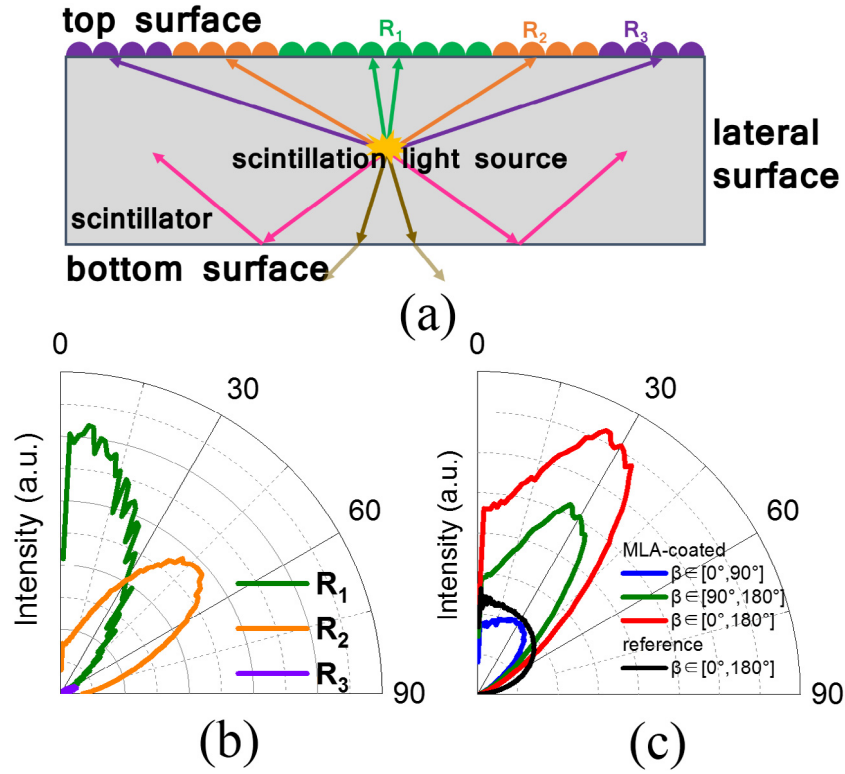


Fig. 3. (a) Schematic illustration of representative light ray paths for different regions. (b) Spatial distribution profiles of light intensity for the regions of R_1 , R_2 and R_3 . (c) Spatial distribution profiles of light intensity for the whole range of β including the downward emission.

where, I_T is the angle-integrated intensity, and I_{θ_A} is the intensity at the azimuth angle of θ_A . When the parameter V reaches its maximum value, it means that not only a strong dependence on this angle is obtained, but also the overall light intensity is as strong as possible under such conditions. Therefore, V can characterize the angle-dependence of light output, concurrently taking into account the total intensity of light output.

3. Results and discussion

As an example, $\text{Bi}_4\text{Ge}_3\text{O}_{12}$ crystals ($n_1 = 2.15$) are selected as the studied scintillators with the size of $18 \times 18 \times 3 \text{ cm}^3$. MLAs made of polystyrene ($n_2 = 1.59$) are coated on the surface of the scintillators. The diameter of an individual microlens is set to be $D = 10 \mu\text{m}$ which is much larger than the emission wavelength of the $\text{Bi}_4\text{Ge}_3\text{O}_{12}$ scintillators so that the ray-optics is applicable. A crystal with the identical size is selected as a reference sample without MLAs.

For an isolated microlens, when light rays reach the boundary of the microlens, the spatial distribution of light intensity forms an escape cone which has a symmetry axis shown in Fig. 2(a). While for a MLA, the spatial distribution of light intensity will be affected by the surrounding microlenses. According to Appendix A, the magnitude of γ_{\max} and β will determine the direction of symmetry axis. Therefore, it is necessary to divide the range of β into three regions of β_1 , β_2 , and β_3 , which can be defined by the formula (2). In the range of β_1 , an overlap appears, while in the range of β_3 , the symmetry of distribution will be broken because of the surrounding microlenses.

$$\begin{cases} \beta_1 : 0 < \beta < 27.72^\circ (\frac{1}{2}\gamma_{\max}) \\ \beta_2 : 27.72^\circ < \beta < 60^\circ (90^\circ - \arcsin \frac{1}{2}) \\ \beta_3 : \beta > 60^\circ \end{cases} \quad (2)$$

The simulated spatial distribution of light intensity for an isolated microlens at three representative angles in each region is shown in

Fig. 2(b), which indicates an obviously different spatial distribution in different β regions. In the range of β_1 , the light rays close to the normal direction are defined as inward light rays, and the light rays far away from the normal direction are defined as outward light rays, as shown in Fig. 2(c). The simulated results shown in Fig. 2(d) suggest that the overlap region containing both of the inward and the outward light rays leads to the symmetry axis along the normal direction. In the range of β_2 , the spatial distribution of light intensity exhibits a symmetrical pattern along the symmetry axis. While in the range of β_3 , the transmitted light rays would be obscured and reflected into the crystal by the surrounding microlenses, as shown in Fig. 2(e). The simulated spatial distribution of light intensity for the transmitted light and the refracted light is shown in Fig. 2(f).

Due to the significantly different spatial distribution for the regions of β_1 , β_2 , and β_3 , the top surface should be accordingly divided into three regions of R_1 , R_2 and R_3 , as shown in Fig. 3(a). Fig. 3(b) presents the spatial distribution profiles of light intensity for the regions of R_1 , R_2 and R_3 , which is an angle-integral intensity with their corresponding ranges of β_1 , β_2 , and β_3 . For the sake of simplicity, we only plot the unilateral angle. Firstly, for the R_1 region, the maximum intensity appears at the angle of 0° with a rapid decrease for an increasing angle. Secondly, for the R_2 region, the spatial distribution of light intensity has a maximum intensity around the angle of 45° . Finally, the impact of the surrounding microlenses in the R_3 region will restrict severely the light extraction efficiency, making the R_3 region little contribution to the total light output.

In the above discussion, we only consider the upward emitted scintillation light for $\beta \in [0^\circ, 90^\circ]$. However, the downward emitted scintillation light rays for $\beta \in [90^\circ, 180^\circ]$ will be reflected by the lateral and bottom surfaces and thus have chances to reach the top surface. As a result, the reflected light rays could be extracted with the assistance of the lateral and bottom surfaces. It is therefore essential to consider the multiple reflections by the lateral and bottom surfaces. Fig. 3(c) displays the spatial distribution of light intensity, including the contributions from the upward light and the downward light. It is interesting

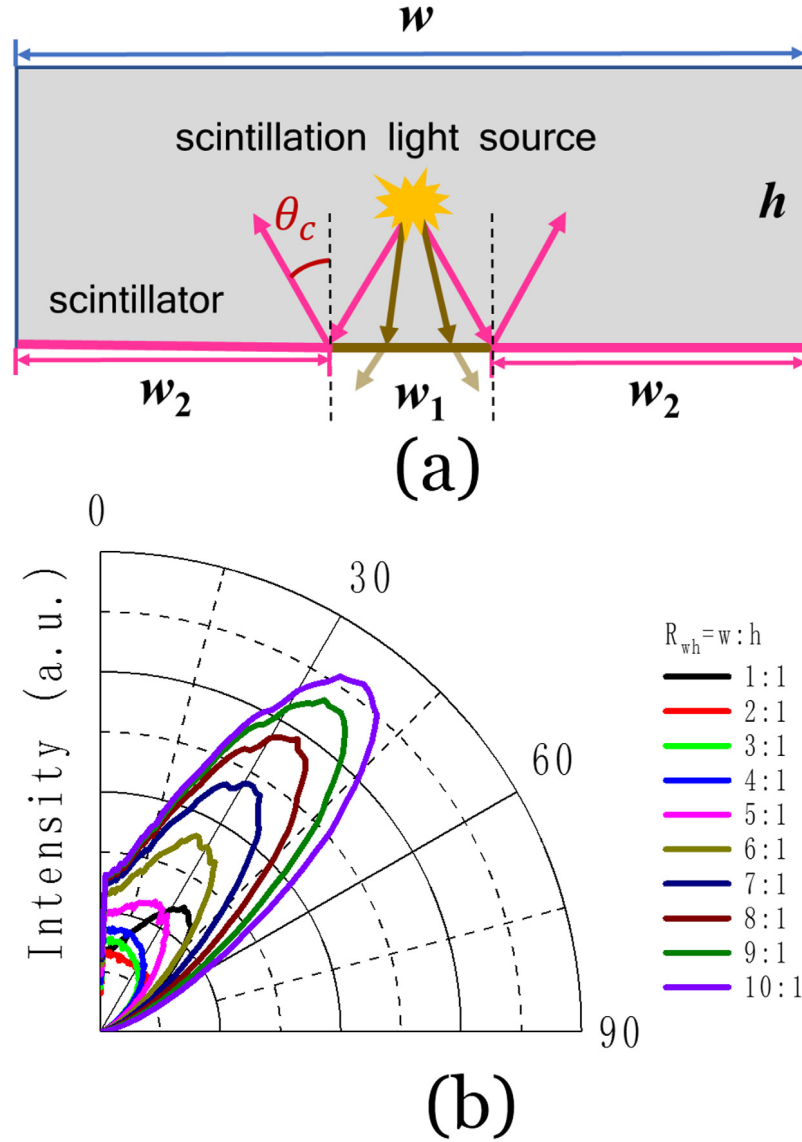


Fig. 4. (a) Schematic illustration of representative light ray paths while hitting the bottom surface. Here, θ_c is the critical angle, w is the width, h is the thickness, and w_1 (w_2) is the width corresponding to the region below (beyond) the critical angle. (b) Spatial distribution of light intensity for different values of R_{wh} .

to find that the contribution from the downward light is dominant. This consideration is analogy to an actual situation. Compared with the reference scintillator without MLAs, a 2.02-fold angle-integrated enhancement is obtained. Additionally, the directionality of emission controlled by MLAs exhibits a broad angular range, which is influenced by the thickness of scintillator due to the average effect.

The above results are obtained for the scintillator with a specific size. However, we have found that the multiple reflections by the lateral and bottom surfaces have a marked impact on the ultimate light output. It is thus expected that the ratio of width (w) and thickness (h) (labeled as $R_{wh} = w/h$) plays an important role. Fig. 4(a) presents the representative light ray paths while hitting the bottom surface. Here, θ_c is the critical angle, w is the width, h is the thickness, and w_1 (w_2) is the width corresponding to the region below (beyond) the critical angle. For $\beta < \theta_c$, most of the light rays will transmit through the bottom surface, and only a small fraction of light rays will encounter Fresnel reflection at the bottom surface. While for $\beta > \theta_c$, the light rays will be totally reflected by the bottom surface. If h is fixed, when w increases, w_1 remains unchanged, but w_2 also increases. As a result, when R_{wh} increases, the light extraction efficiency will be greatly improved due to the increased light rays reflected by the bottom surface. In addition,

because a part of light rays are refracted into air through the bottom surface, the intensity around the normal direction reduces, thus making the maximum intensity concentrate on the range of angle from 30° to 45°.

The spatial distribution of light intensity for different values of R_{wh} is simulated with a fixed h value of 3 cm and variable w values. As shown in Fig. 4(b), it is found that for $R_{wh} = 1$, the light rays usually escape from the lateral surface but seldom reflect at the bottom surface, leading to the maximum intensity at 35°. When the values of R_{wh} increase to 2, 3 or 4, the lateral surface will reflect a part of light rays, leading to the maximum intensity at about 0°. However, when the values of R_{wh} continuously increase to 5 or larger, the intensity of reflected light rays by the lateral surface is much less than that by the bottom surface. As a consequence, the angle for maximum intensity will change to about 45°. Compared to the case of $R_{wh} = 1$, the angle-integrated enhancement ratio reaches 2.51 for the case of $R_{wh} = 10$.

In order to understand the impact of the refractive index of micro-lens n_2 on the extraction efficiency and the control of directional emission, the simulated results for different values of n_2 are presented in Fig. 5. The case for $n_2 = 1.0$ can be regarded as a reference case. As

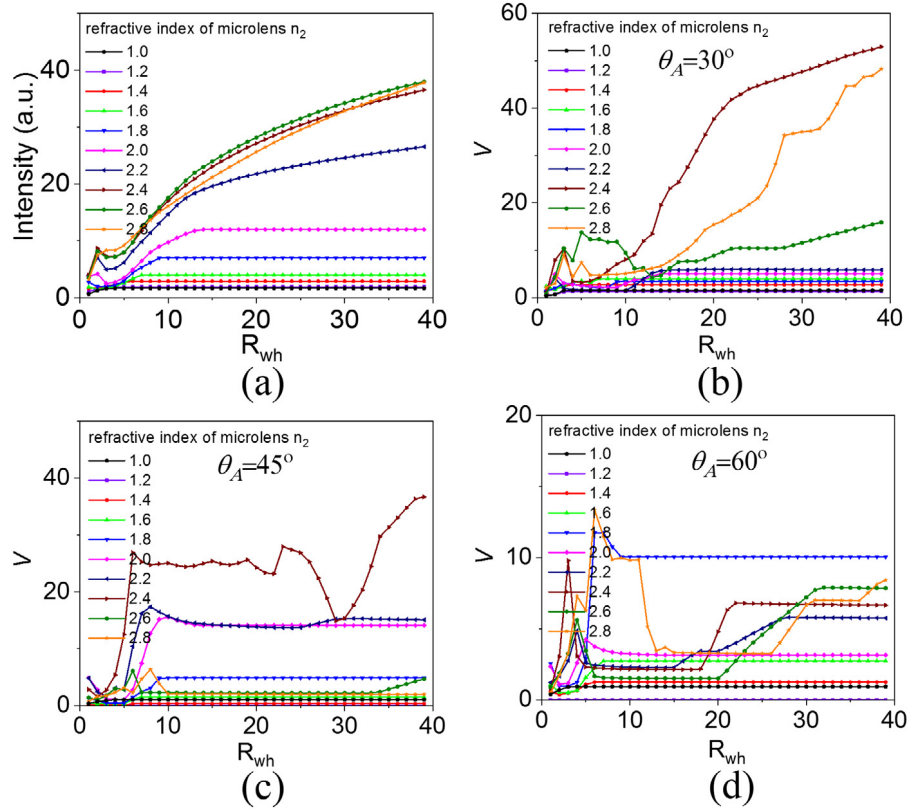


Fig. 5. (a) Angle-integrated intensity with a function of R_{wh} for different refractive indices of microlens n_2 . (b), (c) and (d) V values with a function of R_{wh} for different refractive indices of microlens n_2 with the emission angles at 30° , 45° and 60° , respectively.

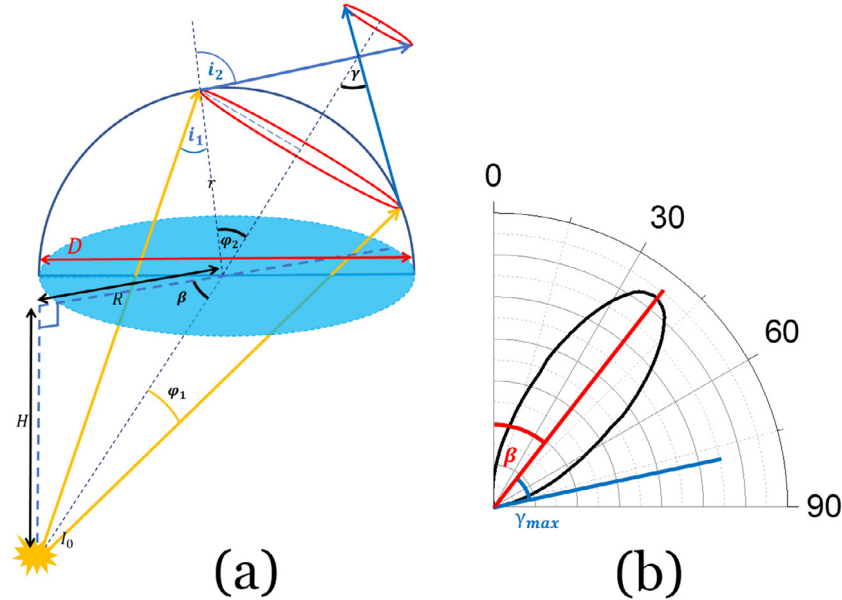


Fig. 6. (a) Definition of the related parameters in an individual microlens. (b) Spatial distribution of light intensity of an individual microlens.

shown in Fig. 5(a), when the values of n_2 are between 1.0 and 1.2, the angle-integrated intensity first increases and then stabilizes when $R_{wh} > 5$. When the values of n_2 is between 1.4 and 1.8, the angle-integrated intensity first decreases and then increases to a stable value when $R_{wh} > 9$. While, when the values of n_2 are larger than 2.0, the angle-integrated intensity exhibits a continuous increase with the increasing values of R_{wh} , except for a small dip at $R_{wh} = 5$. Large values of n_2 are beneficial to the enhancement of light extraction efficiency, especially for the

cases with large values of R_{wh} . For example, one can find that when $R_{wh} = 2$, a 6.86-fold enhancement can be obtained with $n_2 = 2.4$, while when $R_{wh} = 39$, a 22.6-fold enhancement can be obtained with $n_2 = 2.6$. It is interesting to find that the maximum angle-integrated intensity could be obtained when the values of n_2 are slightly larger than those of scintillators. The main reason is that at this situation the scintillation light rays could easily enter the microlens. However, when the values of n_2 are much larger than those of scintillators, the light rays inside the

Table 1
Optimal parameters for the maximum values of V .

| θ_A | n_2 | R_{wh} | V_{max} |
|------------|-------|----------|-----------|
| 30° | 2.44 | 38.06 | 48.26 |
| 45° | 2.47 | 37.89 | 36.85 |
| 60° | 1.86 | 9.08 | 11.73 |

microlens may be reflected at the interface of air, leading to reduction of light extraction efficiency.

Fig. 5(b), (c) and (d) show the simulated V values with a function of R_{wh} for different refractive indices of microlens n_2 with the emission angles at 30°, 45° and 60°, respectively. The results indicate that the values of n_2 can significantly control the directional emission, which is also strongly dependent on the values of R_{wh} . For the cases of $\theta_A = 30^\circ$ and 45°, the highest values of V are obtained with $n_2 = 2.4$, which is mainly contributed from the high total intensity. When n_2 is larger than n_1 , the directivity of emission is close to the normal direction. As shown in Fig. 5(d), for a large emission angle of 60°, the values of V become very small, compared with the cases of 30° and 45°. Moreover, it is also found that for large values of R_{wh} , the values of V decrease first and then increase, which could be due to the fact that the light rays focus on low angles for small values of R_{wh} , but distributed at high angles for large values of R_{wh} .

The optimal parameters for the maximum values of V shown in Table 1 are determined by genetic algorithms [21]. The optimal values of n_2 are 2.44, 2.47 and 1.86 for the target emission angles of 30°, 45° and 60°, respectively, which are basically consistent with the results in Fig. 5.

4. Conclusion

The present simulations demonstrate that MLAs can be used to increase the extraction efficiency and control the directional emission of scintillation light. Individual microlenses in different regions lead to different propagation behaviors of light rays. To understand the ultimate directional emission, the impact of lateral and bottom surfaces should be correctly considered, which implies that the multiple reflections by the lateral and bottom surfaces play important roles. The control of emission by MLAs is also strongly affected by the ratios of width and thickness of scintillators. It is found that the maximum angle-integrated intensity could be obtained when the refractive indices of microlenses are slightly larger than those of scintillators. The optimal parameters for the MLAs can be obtained by using genetic algorithms.

CRediT authorship contribution statement

Yaozhen Guo: Conceptualization, Investigation, Software, Writing - original draft. **Di Yuan:** Investigation. **Zhongrui Li:** Data curation, Formal analysis, Software. **Chenyu Zhu:** Data curation, Formal analysis, Software. **Zixuan Dai:** Data curation, Formal analysis, Software. **Bo Liu:** Funding acquisition, Methodology, Project administration, Supervision, Writing - review & editing.

Acknowledgments

This work is supported by the National Natural Science Foundation of China (Grant No. 11975168) and the Open Project of the State Key Laboratory of Intense Pulsed Radiation Simulation and Effect (Grant No. SKLIPR2022).

Declaration of competing interest

The authors declare that they have no known competing financial interests or personal relationships that could have appeared to influence the work reported in this paper.

Appendix A. Calculation details for the light intensity distribution of an individual microlens

As shown in Fig. 6(a), the vertical and horizontal distances between scintillation light source and microlens are defined as H and R , respectively. φ_1 denotes the half-apex angle of the escape cone. $\beta = \arctan(H/R)$ is the angle at the symmetry axis of the escape cone. i_1 and i_2 are the incident and emergence angles, respectively. We have the geometrical relationship with formula (3).

$$\frac{\sin(\beta + \varphi_2 - i_1)}{r} = \frac{\sin(\beta) \sin(\beta + \varphi_1)}{\sin(\varphi_1) \sqrt{H^2 + R^2}} \quad (3)$$

According to the law of refraction, we have $i_2 = \arcsin[n_2 \sin(i_1)]$. Thus, we can obtain the expression of light intensity of an individual microlens by formula (4).

$$I'_0 = \frac{I_0}{2} \left[\frac{\sin(2i_1) \sin(2i_2)}{\sin^2(i_1 + i_2)} + \frac{\sin(2i_1) \sin(2i_2)}{\sin^2(i_1 + i_2) \cos^2(i_1 - i_2)} \right] \quad (4)$$

The spatial distribution of this individual microlens is shown in Fig. 6(b). Where, the distribution is symmetric about angle β . And the maximum range of the distribution (γ_{max}) is calculated by formula (5).

$$\gamma_{max} = \arcsin \frac{1}{n_2} + \arcsin \frac{D/2}{n_1 \sqrt{H^2 + R^2}} \quad (5)$$

Therefore, the angle β determines the direction of the symmetry axis and the γ_{max} determines the size of escape cone. When $\beta < \gamma_{max}$, negative-angle distribution appears, which overlaps with other distribution.

Appendix B. Transformation of coordinates

A transformational equation is used to correct the relative position between the scintillation light source and the center of the individual microlens, which is related to the projection of the escape cone onto the plane. Fig. 7 shows the coordinate systems before and after transformation. An orthogonal transformation matrix is given by formula (6). Where, φ_3 is the inclination angle of an inclined ellipse. This is a standard method to transform a normal ellipse into an inclined ellipse [22].

$$\begin{bmatrix} x' \\ y' \end{bmatrix} = \begin{bmatrix} \cos \varphi_3 & -\sin \varphi_3 \\ \sin \varphi_3 & \cos \varphi_3 \end{bmatrix} \begin{bmatrix} x \\ y \end{bmatrix} \quad (6)$$

Thus, the transfer equation can be given by formula (7).

$$\begin{cases} x = r' \cos(\theta + \frac{\pi}{2}) \cos(\varphi_3) - r' \cos(\varphi_1) \sin(\theta + \frac{\pi}{2}) \sin(\varphi_3) \\ y = r' \cos(\theta + \frac{\pi}{2}) \sin(\varphi_3) + r' \cos(\varphi_1) \sin(\theta + \frac{\pi}{2}) \cos(\varphi_3) \\ z = h - \frac{r}{H}(x + y) \\ r' = r \sin(\varphi_2) \\ \theta \in (0, 2\pi) \\ \varphi_2 \in (0, \varphi_{2-max}) \end{cases} \quad (7)$$

Appendix C. Genetic algorithms and operational logic

The genetic algorithms have six steps: encoding, swap, mutation, inversion, evaluation and copy. In the encoding step, the variables are encoded to binary series which have length of k . The binary form of variables also could be called as gene. The relationship between the binary form of $b_k b_{k-1} \dots b_3 b_2 b_1$ and the origin value of x is as below.

$$x = L = \left(\sum_{i=1}^k b_i 2^{i-1} \right) \left(\frac{U-L}{2^k - 1} \right) \quad (8)$$

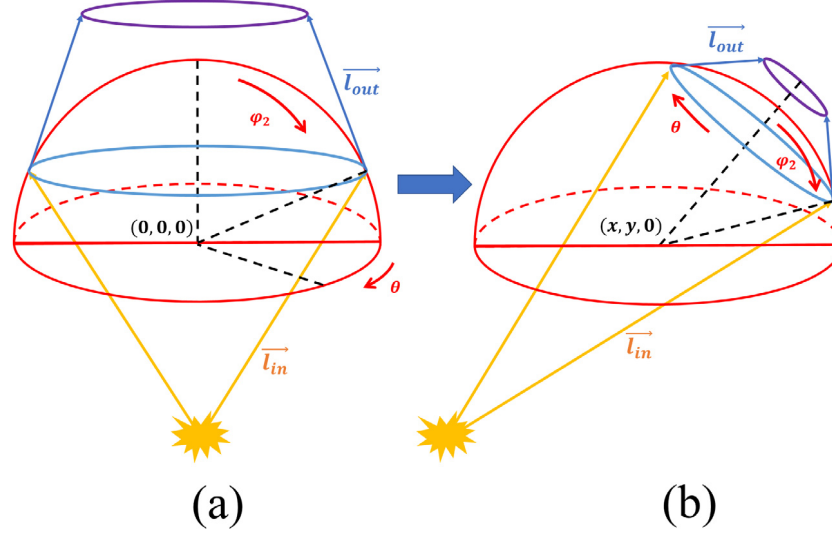


Fig. 7. (a) Coordinate system before transformation. (b) Coordinate system after transformation.

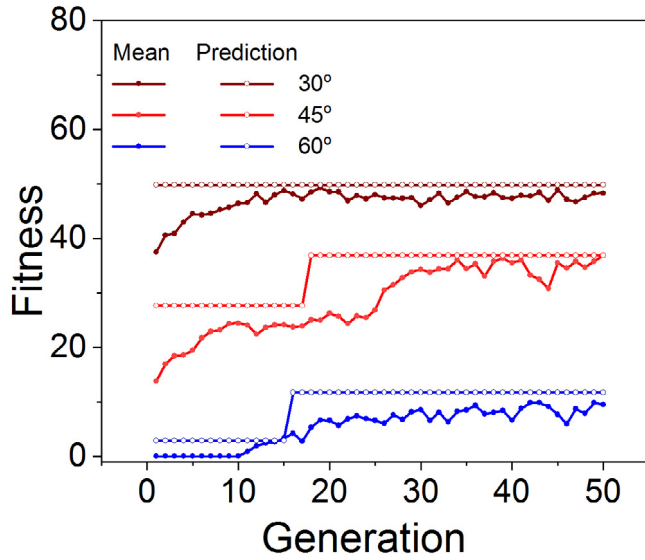


Fig. 8. Fitness-generation curve in the genetic algorithms.

Where U and L are the upper bound and the lower bound of the variables, respectively. The precision of variables can be expressed as formula (9).

$$\delta = \frac{U - L}{2^k - 1} \quad (9)$$

The swap process starts after the encoding process has finished. In this process, two genes are selected randomly from gene pools. The part of genes will be swap by generating a random swap point. In the mutation process, a gene is chosen randomly, followed by a change of value in a random point. In the inversion process, the order of a gene will be inverted from a randomly selected start point. Next, the genes will be decoded, then the values of a target function will be calculated. In order to minimize the target function, the evaluation number is defined as formula (10).

$$eval = small_{num} + f(x_1, x_2) \quad (10)$$

The probability of copying to next generation of a gene is:

$$P_i = \frac{eval_i}{\sum_j eval_j} \quad (11)$$

The accumulated probability of a gene is:

$$Q_j = \sum_j P_j \quad (12)$$

Finally, a series of random numbers in $[0, 1]$ will be generated, a gene Q_i will be copied to the next generation if and only if:

$$Q_i < rand \leq Q_{i+1} \quad (13)$$

Where, $rand$ is a random number from 0 to 1. Apparently, the less the target value is, the larger the probability of copy is. After a sufficient number of iterations, the group will converge finally. Fig. 8 displays the fitness curve for values of V , the fitness converges to the predicted curve and thus the calculated result is of great reference value.

References

- [1] Q. Li, X. Liu, M. Gu, Y. Hu, F. Li, S. Liu, Q. Wu, Z. Sun, J. Zhang, S. Huang, Opt. Express 26 (2018) 31290–31298.
- [2] H. Chen, M. Gu, Z. Sun, X. Liu, B. Liu, J. Zhang, S. Huang, C. Ni, Opt. Express 27 (2019) 14871–14880.
- [3] A. Chilingarian, G. Hovsepyan, E. Mnatsakanyan, Phys. Rev. D 93 (2016) 052006.
- [4] W. Heiss, C. Brabec, Nature Photonics 10 (2016) 288.
- [5] C. Struening, J. Chong, G. Lee, M. Zavala, A. Erickson, Y. Ding, C.-L. Wang, Y. Diawara, R. Engels, B. Wagner, Appl. Phys. Lett. 108 (2016) 153106.
- [6] M. Nikl, A. Yoshikawa, Adv. Opt. Mater. 3 (2015) 463–481.
- [7] X. Chen, B. Liu, Q. Wu, Z. Zhu, J. Zhu, M. Gu, H. Chen, J. Liu, L. Chen, X. Ouyang, Opt. Express 26 (2018) 11438–11446.
- [8] J. Liu, B. Liu, Z. Zhu, L. Chen, J. Hu, M. Xu, C. Cheng, X. Ouyang, Z. Zhang, J. Ruan, Opt. Lett. 42 (2017) 987–990.
- [9] M. Salomoni, R. Pots, P. Lecoq, E. Auffray, S. Gundacker, M. Paganoni, B. Singh, M. Marshall, V.V. Nagarkar, IEEE Trans. Nucl. Sci. 65 (2018) 2191–2195.
- [10] M. Salomoni, R. Pots, E. Auffray, P. Lecoq, Crystals 8 (2018) 78.
- [11] Z. Zhu, B. Liu, C. Cheng, H. Zhang, H. Chen, M. Gu, J. Liu, L. Chen, X. Ouyang, C. Xue, Appl. Phys. Lett. 110 (2017) 051901.
- [12] B. Liu, Q. Wu, Z. Zhu, C. Cheng, M. Gu, J. Xu, H. Chen, J. Liu, L. Chen, Z. Zhang, Appl. Phys. Lett. 111 (2017) 081904.
- [13] B. Liu, Z. Zhu, J. Zhu, S. Wu, H. Chen, M. Gu, Q. Cheng, H. Chen, C. Cheng, Z. Wang, Appl. Phys. Lett. 104 (2014) 061902.
- [14] B. Liu, Z. Zhu, Q. Wu, C. Cheng, M. Gu, J. Xu, H. Chen, J. Liu, L. Chen, X. Ouyang, Appl. Phys. Lett. 110 (2017) 181905.
- [15] S.-I. Chang, J.-B. Yoon, H. Kim, J.-J. Kim, B.-K. Lee, D.H. Shin, Opt. Lett. 31 (2006) 3016–3018.
- [16] X.-H. Lee, I. Moreno, C.-C. Sun, Opt. Express 21 (2013) 10612–10621.
- [17] Y.M. Song, Y. Xie, V. Malyarchuk, J. Xiao, I. Jung, K.-J. Choi, Z. Liu, H. Park, C. Lu, R.-H. Kim, Nature 497 (2013) 95–99.
- [18] H.S. Kim, S.I. Moon, D.E. Hwang, K.W. Jeong, C.K. Kim, D.-G. Moon, C. Hong, Opt. Laser Technol. 77 (2016) 104–110.
- [19] K. Binder, D.W. Heermann, Comput. Phys. 7 (1988) 156.
- [20] U. Maulik, S. Bandyopadhyay, Pattern Recognit. 33 (2000) 1455–1465.
- [21] V. Kreinovich, C. Quintana, O. Fuentes, Cybern. Syst. 24 (1993) 9–26.
- [22] E. Kovács, Ann. Math. Inform. 40 (2012) 175–186.